Tuning low-temperature physical properties of $CeNiGe_3$ by magnetic field

E. D. Mun, S. L. Bud'ko, A. Kreyssig, and P. C. Canfield
Ames Laboratory US DOE and Department of Physics and Astronomy, Iowa State University, Ames, Iowa 50011, USA
(Received 21 May 2010; revised manuscript received 8 July 2010; published 18 August 2010)

We have studied the thermal, magnetic, and electrical properties of the ternary intermetallic system $CeNiGe_3$ by means of specific heat, magnetization, and resistivity measurements. The specific heat data, together with the anisotropic magnetic susceptibility, was analyzed on the basis of the point charge model of crystalline electric field. The $J=5/2$ multiplet of the Ce^{3+} is split by the crystalline electric field into three Kramers doublets, where the second and third doublets are separated from the first (ground state) doublet by $\Delta_1 \sim 100$ K and $\Delta_2 \sim 170$ K, respectively. In zero field $CeNiGe_3$ exhibits an antiferromangeic order below $T_N = 5.0$ K. For $\mathbf{H} \| \mathbf{a}$ two metamagnetic transitions are clearly evidenced between 2–4 K from the magnetization isotherm and extended down to 0.4 K from the magnetoresistance measurements. For $\mathbf{H} \| \mathbf{a}$, T_N shifts to lower temperature as magnetic field increases, and ultimately disappears at $H_c \sim 32.5$ kOe. For $H > H_c$, the electrical resistivity shows the quadratic temperature dependence ($\Delta\rho = AT^2$). For $H \gg H_c$, an unconventional T^n dependence of $\Delta\rho$ with $n > 2$ emerges, the exponent n becomes larger as magnetic field increases. Although the antiferromagnetic phase transition temperature in $CeNiGe_3$ can be continuously suppressed to zero, it provides an example of field tuning that does not match current simple models of quantum criticality.

DOI: 10.1103/PhysRevB.82.054424 PACS number(s): 75.30.Kz, 75.30.Mb, 75.50.Ee

I. INTRODUCTION

The ground state of Ce-based intermetallic compounds is often determined by a competition between the intersite Ruderman-Kittel-Kasuya-Yosida (RKKY) interaction and the on-site Kondo fluctuation, a competition that leads to a plethora of unusual ground states. Depending on the strength of the hybridization between $4f$ and conduction electrons relative to their coupling strength, the ground states broadly occur either as magnetically ordered or nonmagnetic (paramagnetic). In addition to these two interactions, the crystalline electric field (CEF) plays a significant role in determining the temperature-dependent thermodynamic and transport properties. With increasing hybridization, the magnetic moments associated with localized $4f$ electrons are increasingly screened by the conduction electrons, leading to a reduction in magnetic moments.[1] The strength of the hybridization can be varied by suitable control parameters, such as pressure (P), composition (x), and magnetic field (H). A quantum critical point (QCP) can be approached by tuning the second-order phase transition temperature down toward $T \to 0$ K with an external, nonthermal, control parameters (P,x,H).[2,3] Of these three parameters, magnetic field is often considered to be an ideal control parameter, since it can be reversibly, and continuously, used to tune the system toward the QCP. Many antiferromagnetic (AFM) heavy fermion (HF) compounds with field-induced QCP have been identified and exhibit prominent non-Fermi-liquid (nFL) behavior expanding out (to higher temperature) from the QCP, triggered by quantum fluctuations.[4–9]

$CeNiGe_3$ has been studied and identified as an AFM Kondo system.[10] Strong anisotropy in thermodynamic and transport properties can be expected from the crystal structure; $CeNiGe_3$ crystallizes in the orthorhombic $SmNiGe_3$-type structure (*Cmmm*, No. 65) with lattice parameters $a=4.139$ Å, $b=21.828$ Å, and $c=4.1723$ Å.[10,11] A layered structure, $CeNiGe_3$ is assembled by a sequence Ge_2Ni-$CeGe_2Ce$-$NiGe_2$ layers along the **b** axis.[10,12] In this structure, Ce occupies a single $4j$ site with $mm2$ point symmetry. At ambient pressure and in zero field, $CeNiGe_3$ shows AFM order below $T_N=5.5$ K.[10,13–15] Recent studies of polycrystalline $CeNiGe_3$ (Ref. 10) have inferred that the AFM order can be suppressed by external magnetic field, via metamagnetic transitions (MMTs). Although polycrystalline samples can show intrinsic property of materials with directional averaged value, single crystals are needed for reliable H-T phase diagrams of magnetically anisotropic compounds. More recently, pressure-induced superconductivity was found in electrical resistivity measurements on polycrystalline samples[13,14] and in specific heat (ac calorimetry) measurements on single crystal samples.[15] These studies indicate that the RKKY and/or Kondo interaction can be tuned by applied pressure and superconductivity can be induced in this Kondo system.

In order to gain insight into the anisotropic, low-temperature physical properties of $CeNiGe_3$, we have grown single crystals and performed thermodynamic and transport measurements in applied magnetic fields up to 90 kOe. In this paper specific heat, electrical resistivity, and magnetization measurements on single crystal $CeNiGe_3$ as function of temperature and magnetic field are presented. A strong magnetic anisotropy is observed and can be reproduced by CEF analysis, and two-step MMTs are clearly observed in the magnetization isotherms and magnetoresistance data. The constructed H-T phase diagram of $CeNiGe_3$, for applied magnetic field along the magnetically easy axis, $\mathbf{H} \| \mathbf{a}$, is qualitatively in agreement with a previous polycrystalline sample study[10] and is also similar to the case of $CeAuSb_2$ (Ref. 6) and the isostructural compound $YbNiSi_3$ (Ref. 16) in which the AFM order is also suppressed by applied magnetic field via MMTs.

II. EXPERIMENTAL

Single crystals of $RNiGe_3$ (R=Ce and Y) were grown via solution growth techniques from a Ni-Ge rich, self-flux using

 ©2010 The American Physical Society

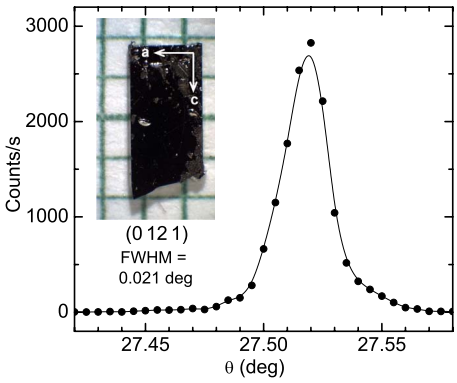

FIG. 1. (Color online) X-ray rocking curve through the (0 12 1) reflection of the $CeNiGe_3$ single crystal. Inset shows a picture of a $CeNiGe_3$ single crystal on millimeter grid paper. The orthorhombic **b** direction is perpendicular to the plate of the crystal. The short (longer) length of the plate is parallel to the orthorhombic **a**(**c**) direction and the longer length of the plate is parallel to the *c* axis. The small droplets on the surface are residual flux that can be polished off before measurements.

high purity starting elements.[17–19] A Ni-Ge-rich self-flux was used because of both the wide range of binary eutectic valley and the merit of introducing no new elements in the growth. The constituent elements, using a starting molar proportion of 1:1.6:9 (R:Ni:Ge), were placed in an alumina crucible and sealed in a silica tube under a partial pressure of Ar. The temperature of the furnace was raised to 1050 °C and after homogenizing the mixture for 2 h, the melt solution was slowly cooled over 100 h down to 780 °C for Ce, 850 °C for Y. After decanting the excess solution, using a centrifuge, thin, platelike crystals were obtained. Samples have shiny, and generally clean, surfaces; small, spotlike, flux droplets solidified on the crystal surface were polished off before physical property measurements.

The crystallographic **b** axis was found to be perpendicular to the plate surface and well formed **a**-**c** edge facets were clearly visible (Fig. 1). The orthorhombic **b** axis was easily determined to be perpendicular to the plate surface by x-ray Laue pattern in reflection geometry. The orthorhombic **a** and **c** directions have been assigned by measurements of the lattice parameters using a four-circle diffractometer with Cu $K_{\alpha 1}$ radiation from a rotating anode x-ray source, selected by a germanium (1 1 1) monochromator. To confirm correct assignment, the reflection conditions according to the space group *Cmmm* has been satisfactorily checked: the (0 12 1) and (0 14 1) reflections have been found in contrast to the observation of pure background signal at what would be the (0 13 1) position, in agreement with the general reflection condition $h+k=2n=$even for (hkl) Bragg reflections. The high quality of the single crystals can be demonstrated by the excellent mosaicity of 0.021° in full width at half maximum for the rocking scan shown in Fig. 1.

Powder x-ray diffraction measurements were taken on a Rigaku MiniFlex at room temperature with Cu $K_{\alpha 1}$ radiation in order to confirm the crystal structure and lattice parameters. We prepared two powder samples of the RNiGe$_3$ (R =Ce and Y) compounds, the first one was for confirming the crystal structure and phase purity, the second one, which was mixed with Si-reference powder for correcting zero shift, was for determining the lattice constants. No secondary phases were detected, except small amount of pure Ge phase coming from residual flux droplets on the crystal surface. After polishing the surface of the samples before grinding, the Ge peaks in the x-ray spectra were no longer present. The refined lattice constants (a=4.1384 Å, b=21.838 Å, and c =4.1695 Å for $CeNiGe_3$ and a=4.0543 Å, b=21.520 Å, and c=4.0617 Å for $YNiGe_3$) are consistent with the earlier studies.[10,11] The structure type, space group, atomic position, and lattice constants of the single crystals of $CeNiGe_3$ and $YNiGe_3$ were also confirmed by single crystal x-ray measurements.[12]

Magnetization was measured as a function of temperature from 1.8 to 300 K and magnetic fields up to 70 kOe in a Quantum Design (QD) Magnetic Property Measurement System (MPMS). Heat capacity was measured in a QD Physical Property Measurement System (PPMS) with ^{3}He option by the relaxation method within the temperature range from 0.4 to 50 K. Electrical resistivity was measured using a standard four-probe ac (f=16 Hz) technique in a QD PPMS down to 0.4 K. The platelike samples were cut with a wire saw (and polished) for resistivity measurements. Electrical contacts were made to the sample using Epotek H20E silver epoxy to attach Pt wires (50 μm diameter). The magnetic field-dependent resistivity was measured in transverse $[(\mathbf{I}\parallel\mathbf{c})\perp(\mathbf{H}\parallel\mathbf{a})]$ configuration for applied fields up to 90 kOe.

III. RESULTS

A. Magnetic susceptibility

The temperature-dependent magnetic susceptibility $\chi(T)=M(T)/H$ and inverse magnetic susceptibility, H=1 kOe, along each principal axis are plotted in Fig. 2(a). $\chi(T)$ for $\mathbf{H}\parallel\mathbf{a}$, which is the magnetic easy axis, shows a sharp peak as a signature of the AFM order. $\chi(T)$ curves for $\mathbf{H}\parallel\mathbf{b}$ and **c** are much smaller than that for $\mathbf{H}\parallel\mathbf{a}$. $\chi(T)$ for each principal axis follows Curie-Weiss law $\chi(T)=\frac{C}{(T-\theta)}$ above 150 K.

The strong magnetic anisotropy is also reflected in the anisotropic Weiss temperature (θ_a=28 K, θ_b=−60 K, and θ_c=−123 K). Even though the crystal structure of $CeNiGe_3$ appears to be "almost tetragonal" with a and c differing by less than 1%, the large difference of θ between magnetic easy and hard axes results from point symmetry of the Ce site. From the polycrystalline averaged susceptibility for $\mathbf{H}\parallel\mathbf{a}$, $\mathbf{H}\parallel\mathbf{b}$, and $\mathbf{H}\parallel\mathbf{c}$, $\chi_{\text{poly}}=\frac{1}{3}(\chi_a+\chi_b+\chi_c)$ [dashed line in Fig. 2(a)], the effective moment $\mu_{\text{eff}}=2.57\mu_B/Ce^{3+}$ and the Weiss temperature $\theta_{\text{poly}}=-21$ K were obtained by fitting the data to the Curie-Weiss law. The inferred effective moment is close to the full Hund's rule (J=5/2) ground-state value, $2.54\mu_B$. $\chi(T)$ deviates from the Curie-Weiss law below 150 K in a manner which suggests that degeneracy of the J =5/2 of Ce^{3+} manifold is lifted by CEF (see CEF analysis below).

The low field, AFM ordering temperature T_N=5.0 K was determined from the maximum of $d\chi\cdot T/dT$ as shown in Fig. 3,[20,21] which is consistent with the peak position of specificheat data. The determined AFM ordering temperature is

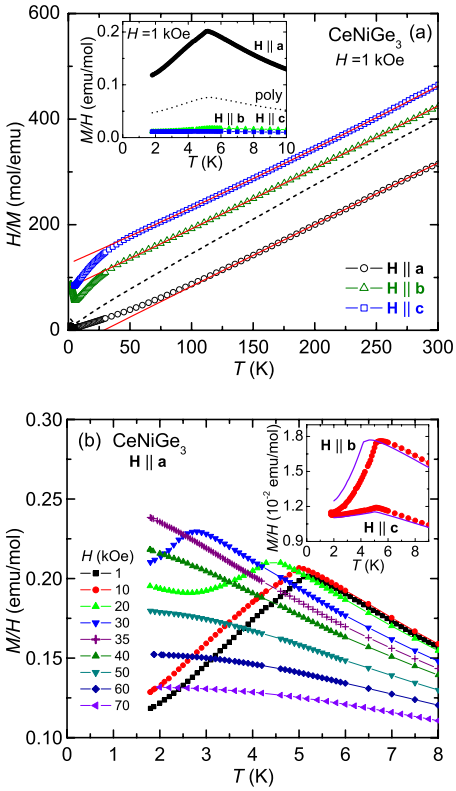

FIG. 2. (Color online) (a) Inverse magnetic susceptibility $H/M(T)$ of $CeNiGe_3$ for each principal axis (open symbols) and the polycrystalline average (dashed line). Solid lines are from the high-temperature Curie-Weiss fits to the data. Inset: magnetic susceptibility below 10 K for $\mathbf{H}\|\mathbf{a}$, polycrystalline average, $\mathbf{H}\|\mathbf{b}$, and $\mathbf{H}\|\mathbf{c}$ (top to bottom). (b) $M(T)/H$ of $CeNiGe_3$ for $\mathbf{H}\|\mathbf{a}$ at selected magnetic fields. Inset: $M(T)/H$ for $\mathbf{H}\|\mathbf{b}$ and $\mathbf{H}\|\mathbf{c}$ at $H=10$ kOe (symbols) and 70 kOe (lines).

lower than the previously reported value $T_N=5.5$ K.[10,13–15] The low-temperature $\chi(T)$ data, measured for $\mathbf{H}\|\mathbf{a}$, are plotted for various applied fields in Fig. 2(b). With increasing magnetic field, T_N shifts to lower temperatures and drops below 2 K for $H\geq 35$ kOe. At higher fields, $\chi(T)$ does not reveal any signature of phase transitions and instead shows a

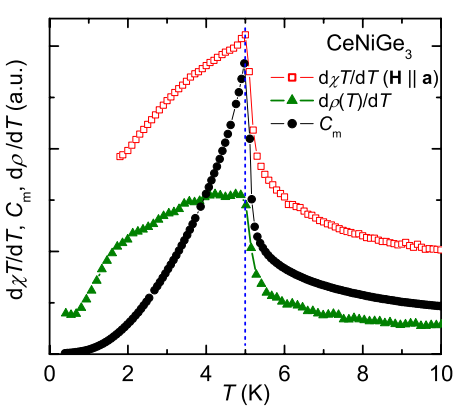

FIG. 3. (Color online) Low-temperature $d\chi T/dT$ for $H=1$ kOe, C_m, and $d\rho(T)/dT$ for $CeNiGe_3$. The antiferromagnetic ordering temperature marked by dotted line shows up as a sharp, well-defined peak in all three plots.

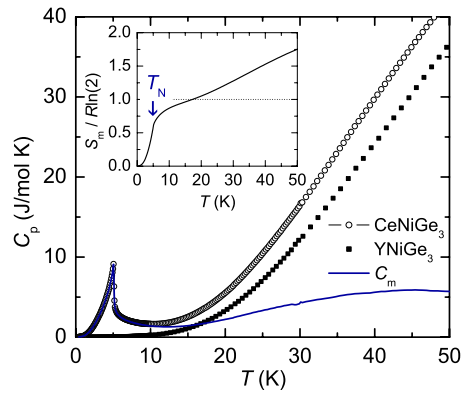

FIG. 4. (Color online) Specific heat of $CeNiGe_3$ and $YNiGe_3$ single crystal and the magnetic specific of $CeNiGe_3$ (see text). Inset: magnetic entropy divided by $R\ln(2)$. The vertical arrow indicates the AFM ordering temperature.

tendency toward saturation at low temperatures. For $\mathbf{H}\|\mathbf{b}$ and $\mathbf{H}\|\mathbf{c}$, however, T_N is hardly affected by applied magnetic field as shown in the inset of Fig. 2(b); at $H=70$ kOe, from the maximum of $d\chi\cdot T/dT$, the determined AFM ordering temperature shifts to $T_N=4.1$ K for $\mathbf{H}\|\mathbf{b}$ and $T_N=4.9$ K for $\mathbf{H}\|\mathbf{c}$.

B. Specific heat

Figure 4 shows the temperature-dependent specific heat C_p of $CeNiGe_3$ and its nonmagnetic, isostructural analog, $YNiGe_3$. There is a large difference in C_p between $CeNiGe_3$ and $YNiGe_3$ below 50 K measured. For $YNiGe_3$ the electronic specific heat coefficient (γ) and Debye temperature (Θ_D) were estimated using the relation $C_p/T=\gamma+\beta T^2$ by plotting data C_p/T vs T^2; $\gamma=3.6$ mJ/mol K^2 and $\Theta_D=236$ K. The specific heat data for $CeNiGe_3$ manifest a clear, sharp, λ anomaly with a cusp at 5.0 K (see Figs. 4 and 5). Because of the AFM order below 5 K and the high temperature, broad feature associated with CEF effect, γ and Θ_D of $CeNiGe_3$ cannot estimated by using the same relation. C_p/T of $CeNiGe_3$ attained a value of 76 mJ/mol K^2 at 0.4 K, which is larger than that of $YNiGe_3$. The data for $YNiGe_3$ are used to estimate the nonmagnetic contribution to the specific heat of $CeNiGe_3$, where we used a mass-corrected data[22,23] for $YNiGe_3$ to subtract from the C_p data for $CeNiGe_3$. The magnetic specific heat of $CeNiGe_3$, $C_m=C_p(\mathrm{CeNiGe_3})-C_p(\mathrm{YNiGe_3})$, is also plotted in Fig. 4. The C_m data show a broad maximum centered around 45 K, indicating that there is a significant magnetic contribution from Ce^{3+} ions above T_N. This broad peak can be associated with an electronic Schottky contribution due to the CEF splitting of the Hund's rule ground state multiplet.

The magnetic entropy (S_m) was inferred by integrating C_m/T starting from the lowest temperature measured and plotted in the inset of Fig. 4. S_m reaches about 60% of $R\ln(2)$ at T_N and recovers the full doublet, $R\ln(2)$, entropy by 18 K. This suggests that the sharp anomaly at 5.0 K in specific heat stems from the AFM order in a doublet ground state but the ordered moment is already somewhat compensated by the Kondo interaction. At $T=50$ K, the recovered S_m is less than

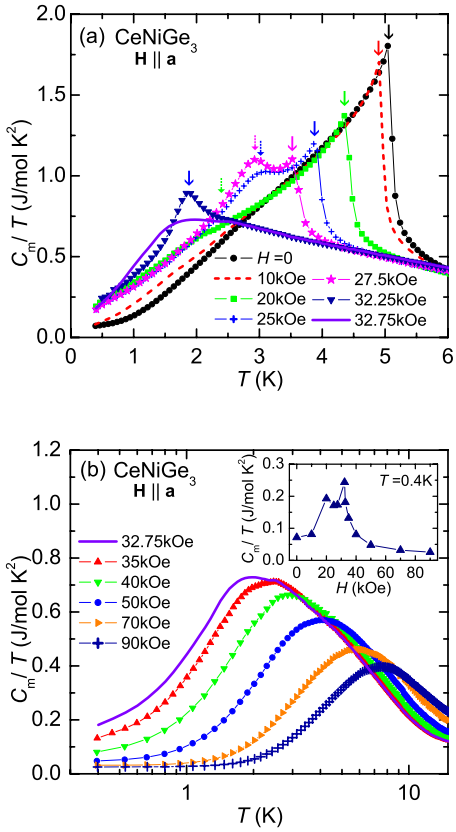

FIG. 5. (Color online) Low-temperature magnetic specific heat divided by temperature, C_m/T, shown for (a) low fields and (b) high fields. Larger arrows in (a) indicate the onset of AFM order and smaller arrows for $H=20$, 25, and 27.5 kOe indicate a low-temperature cusp (see text). The inset of (b) shows C_m/T at 0.4 K plotted as a function of magnetic field.

$R\ln(4)$, which suggests that the first and second excited doublets are separated by more than 50 K from the ground state doublet.

In order to examine the effect of an applied magnetic field on the AFM order, the specific heat was measured with $\mathbf{H}\|\mathbf{a}$ up to 90 kOe and is plotted as C_m/T vs T in Fig. 5. A shift of T_N to lower temperatures is seen for $H<32.5$ kOe and a second, lower temperature, cusp consistent with a second phase transition is observed in the data for $20\leq H<32.25$ kOe. The position of the low-temperature cusp for $H=20$ kOe can be related to the broad minimum developed in $\chi(T)$ [Fig. 2(b)]. For $H=32.75$ kOe the magnetic phase transitions are suppressed and instead C_m/T exhibits a broad maximum centered at ~ 2 K, which marks a crossover from the AFM to paramagnetic state associated with Brillouin-type saturation of the moments. At higher fields, this maximum broadens further and moves to higher temperatures as shown in Fig. 5(b), indicating that the magnetic entropy is removed at higher temperature for larger applied fields. Such a behavior has been found in Kondo lattice systems under magnetic fields and can be reasonably reproduced within the Kondo resonance-level model[24] combined with CEF effect. Note that C_m/T displays no clear indication of a low-temperature $\log(T)$, nFL-like behavior[2,3] for any of the fields measured. For $H=32.75$ kOe, C_m/T has such a temperature dependence over only a limited temperature range, between 2.5 and 5.5 K. The electronic specific-heat coefficient γ, reflecting the effective mass of $4f$ electrons, as given by C_m/T for $T\rightarrow 0$, drops quickly as magnetic field increases. Although at low fields, because of the AFM order, γ cannot be formally defined as C_m/T, C_m/T at 0.4 K is displayed as a function of field in the inset of Fig. 5(b), to provide an estimate of γ. In the paramagnetic state the estimated γ values are less than 0.2 J/mole K^2. Hence, the strength of the hybridization between $4f$ and conduction electrons in $CeNiGe_3$ is relatively weak (f electrons in $CeNiGe_3$ are localized) and it can be destroyed easily by the application of magnetic field, which is evidenced by the value $\gamma=25$ mJ/mole K^2 for $H=90$ kOe.

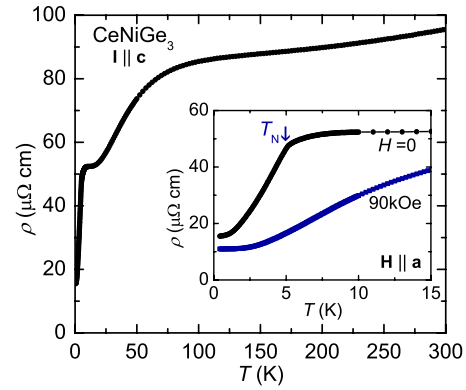

FIG. 6. (Color online) Temperature-dependent electrical resistivity $\rho(T)$ of $CeNiGe_3$. Inset: $\rho(T)$ measured at $H=0$ and 90 kOe for magnetic field applied along $\mathbf{H}\|\mathbf{a}$. The onset of AFM order for $H=0$ is indicated by the arrow.

C. Resistivity

The temperature-dependent resistivity data, $\rho(T)$, of $CeNiGe_3$ are shown in Fig. 6 down to 0.4 K in zero field. There are two broad features in $\rho(T)$ around at 10 and 100 K, the lower one being primarily related to Kondo scattering and the higher one primarily being associated with thermal population of CEF levels. The inset of Fig. 6 shows the zero field $\rho(T)$ below 15 K, together with 90 kOe data for magnetic field $\mathbf{H}\|\mathbf{a}$. The AFM transition manifests itself as a precipitous drop in $\rho(T)$ for $T<T_N$.

From the results of our thermodynamic and transport measurements, the AFM ordering temperature can be clearly determined in $\chi(T)$, $C_p(T)$, and $\rho(T)$. Figure 3 shows $d\chi\cdot T/dT$, $C_m(T)$, and $d\rho(T)/dT$ curves.[20,21] There is an excellent agreement among $d\chi\cdot T/dT=5.0(0)$ K, $C_m(T)=4.9(7)$ K, and $d\rho(T)/dT=4.9(4)$ K. The same analysis to determine phase transition temperatures has been applied to more complex and/or local moment system such as RNi_2B_2C (R=Dy and Ho) (Ref. 25) and shows that the reliable phase transition temperatures can be obtained from thermodynamic and transport measurements.

As magnetic field increases, a gradual suppression of AFM order is observed in $\rho(T)$. The determined AFM phase transition temperatures from $d\rho(T)/dT$ are indicated by arrows in Fig. 7(a). The low-temperature $\rho(T)$ for intermediate

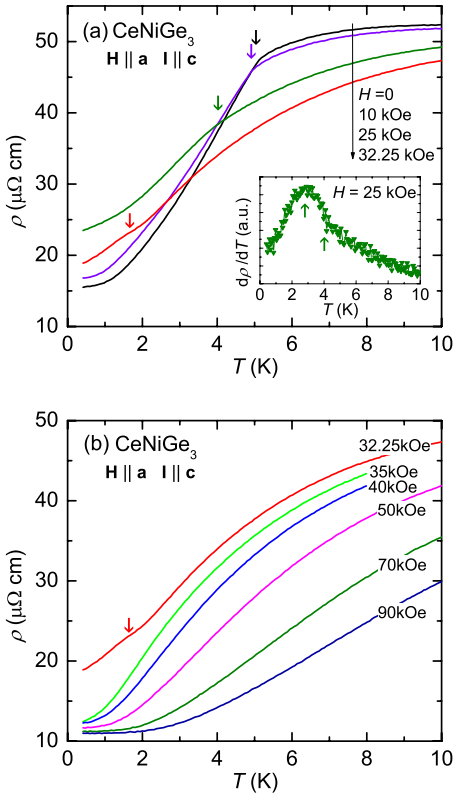

FIG. 7. (Color online) Low-temperature electrical resistivity, $\rho(T)$, at selected magnetic fields applied along $\mathbf{H}\|\mathbf{a}$. (a) $H=0$, 10, 25, and 32.25 kOe. Inset: $d\rho(T)/dT$ for $H=25$ kOe. Arrows indicate a maximum and slope change in $d\rho(T)/dT$. (b) $H=32.25$, 35, 40, 50, 70, and 90 kOe. Arrows indicate the onset of AFM ordering (see text).

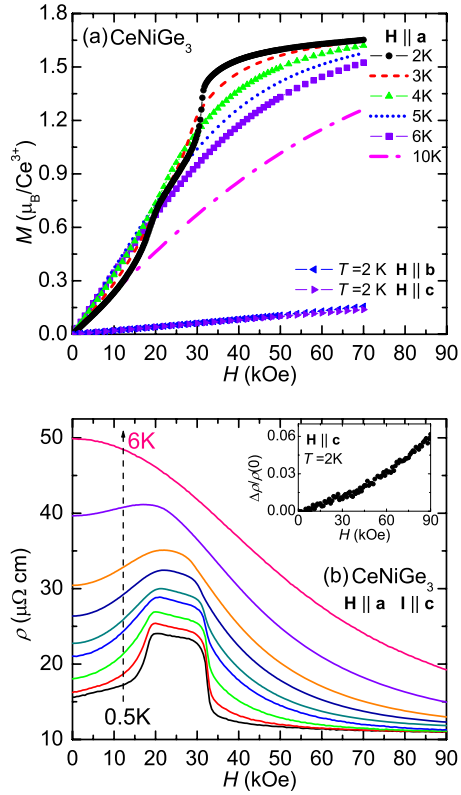

FIG. 8. (Color online) (a) Magnetization isotherms for $\mathbf{H}\|\mathbf{a}$ at $T=2$, 3, 4, 5, 6, and 10 K and for $\mathbf{H}\|\mathbf{b}$ and $\mathbf{H}\|\mathbf{c}$ at 2 K. (b) Electrical resistivity as a function of magnetic field for $\mathbf{H}\|\mathbf{a}$ at $T=0.5$, 1, 1.5, 2, 2.25, 2.75, 3.25, 4.25, and 6 K. Inset: $\rho(H)$ for $\mathbf{H}\|\mathbf{c}$ at 2 K, plotted as $\Delta\rho/\rho(0)$ vs H.

fields, for instance, $H=32.25$ kOe data, reveals more scattering at the phase transition temperature than that in zero field which shows a sharp drop due to loss of spin disorder scattering. The inset of Fig. 7(a) shows the $d\rho(T)/dT$ curve for $H=25$ kOe in which two anomalies can be seen around $\sim$2.8 K as a maximum and $\sim$3.9 K as a slope change. These temperatures are consistent with the cusp and sharp peak position developed in $C_m(T)$ (Fig. 5). At higher fields, FL behavior ($\rho \propto T^2$) is found over a limited range of temperature and field. At very low temperatures and high fields, $\rho(T)$ becomes flat, revealing an anomalous T^n dependence with $n>2$.

D. Magnetization and magnetoresistance

The magnetic field-dependent magnetization, $M(H)$, and resistivity, $\rho(H)$, shed further light on the low-temperature magnetic states of $CeNiGe_3$, as shown in Fig. 8. The observed magnetization isotherms at 2 K are highly anisotropic between $\mathbf{H}\|\mathbf{a}$ and H in the **bc** plane as seen in Fig. 8(a). At 2 K, $M(H)$ for $\mathbf{H}\|\mathbf{b}$ and $\mathbf{H}\|\mathbf{c}$ increases almost linearly up to about $0.15\mu_B/Ce^{3+}$ at 70 kOe. On the other hand, $M(H)$ along $\mathbf{H}\|\mathbf{a}$ linearly increases below 10 kOe and then, undergoes two MMTs and appears to be approaching saturation at 70 kOe with a moment of about $1.65\mu_B/Ce^{3+}$. This value is much higher, by factor of $\sim$4, than in the previous polycrystalline sample study[10] but lower than the theoretical value of $2.14\mu_B$ for the saturated moment of free Ce^{3+} ions. This increase in $M(H)$ takes place via two MMTs at 18.5 and 31 kOe, which are seen as steps in $M(H)$ and also clearly indicated in the $dM(H)/dH$ analysis. Figure 9(a) shows $dM(H)/dH$ at selected temperatures. Two peaks in

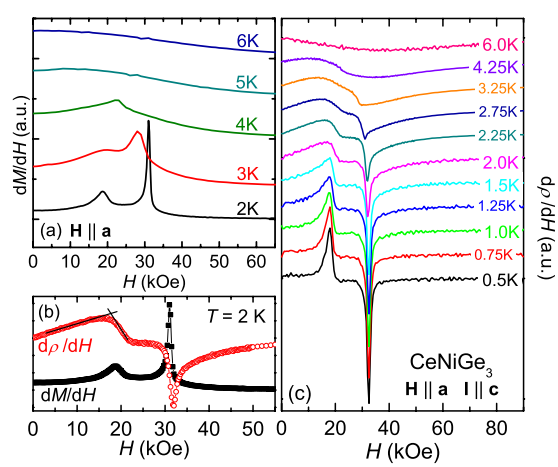

FIG. 9. (Color online) (a) $dM(H)/dH$ for $\mathbf{H}\|\mathbf{a}$ at $T=2$, 3, 4, 5, and 6 K. (b) $d\rho(H)/dH$ and $dM(H)/dH$ at $T=2$ K. Solid lines are guide to eyes. (c) $d\rho(H)/dH$ ($\mathbf{H}\|\mathbf{a}$) at selected temperatures between 0.5 and 6 K.

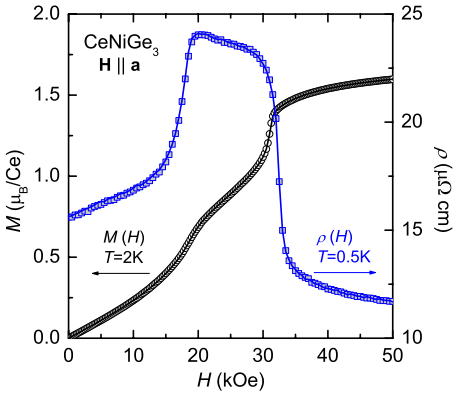

FIG. 10. (Color online) Magnetization isotherms (left axis) at $T=2$ K and magnetoresistivities (right axis) at $T=0.5$ K for $\mathbf{H}\|\mathbf{a}$. Symbols and lines are taken the data with increasing and decreasing magnetic fields, respectively, at fixed temperature.

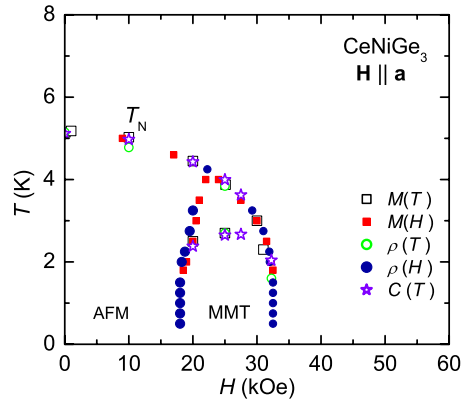

FIG. 11. (Color online) H-T phase diagram of $CeNiGe_3$ for $\mathbf{H}\|\mathbf{a}$. Symbols are taken from temperature and field sweeps using $d\chi\cdot T/dT$, $d\rho(T)/dT$, C_m, $dM(H)/dH$, and $d\rho(H)/dH$ analyses.

$dM(H)/dH$ curves, corresponding to MMTs, are no longer seen for $T\geq 5$ K. For $\mathbf{H}\|\mathbf{b}$ and $\mathbf{H}\|\mathbf{c}$, no MMTs are observed below 70 kOe and down to 2 K.

$\rho(H)$ measurements provide orthogonal cuts through the H-T phase diagram and shed light on some of the features observed in $\rho(T)$. Figure 8(b) presents $\rho(H)$ for $\mathbf{H}\|\mathbf{a}$ below 6 K. Dramatic changes in $\rho(H)$ for $T\leq 4.25$ K reveal the two MMTs while a monotonically decreasing $\rho(H)$ is seen in the 6 K curve up to 90 kOe. Two MMTs are clearly revealed in the $d\rho(H)/dH$ curve as sharp peaks. For comparison $dM(H)/dH$ and $d\rho(H)/dH$ curve at 2 K is plotted in Fig. 9(b). Two MMTs fields revealed at 18 and 31.5 kOe in $d\rho(H)/dH$ are in agreement with the features developed at 18.5 and 31 kOe in $dM(H)/dH$. Below 2 K two MMTs are almost temperature independent while above 2 K the second MMT shifts to lower field as temperature increases. Note that the pronounced steps in $\rho(H)$ were not observed in the polycrystalline sample study.[10] Magnetization at $T=2$ K and magnetoresistivity vs field loops from 0 to 50 kOe at $T=0.5$ K are shown in Fig. 10. Although $CeNiGe_3$ show sharp MMTs, $M(H)$ indicates no hysteresis down to 2 K and no hysteresis is seen in $\rho(H)$ measurements at 0.5 K. In the inset of Fig. 8(b) $\rho(H)$ for $\mathbf{H}\|\mathbf{c}$ at 2 K is plotted as $\Delta\rho/\rho(0)$ vs H. As magnetic field increases $\rho(H)$ increases monotonically without steplike change shown for $\mathbf{H}\|\mathbf{a}$, which is consistent with $M(H)$ results for $\mathbf{H}\|\mathbf{c}$. Below T_N, the observed magnetoresistance (MR) in $CeNiGe_3$ is very similar to that in a tetragonal $CeAuSb_2$ (Ref. 6) and a isostructural $YbNiSi_3$.[16]

IV. DISCUSSION

In Fig. 11 the phase transition temperatures and fields determined from magnetization, resistivity, and specific heat measurements are plotted in the H-T plane, where symbols are extracted from $d\chi\cdot T/dT$, $d\rho(T)/dT$, $dM(H)/dH$, and $d\rho(H)/dH$ analyses, and maximum of $C_m(T)$. The phase transition can be traced by a line which is connected from $T_N=5.0$ K at $H=0$ to the critical field $H_c=32.5$ kOe at $T=0.5$ K. An additional phase boundary emerges below 4 K around 22 kOe. This phase boundary depends weakly on field. Between these two phase boundaries ($20<H<30$ kOe), a nearly temperature-independent phase line seems to exist, which corresponds to the low-temperature cusp observed in C_m (Fig. 5) and the maximum in $d\rho(T)/dT$. At present, it is not clear that the low-temperature cusp in C_m is an indication of phase transition or is associated with an excitation of spin wave. As shown in the phase diagram the critical temperature determined from temperature sweeps track well the critical field determined from field sweeps.

T_N gradually shifts to lower temperature in applied fields up to ~ 30 kOe. It then decreases quickly and seems to be zero near $H_c\sim 32.5$ kOe. In spite of the abrupt changes in the slope of $\rho(H)$, no hysteresis was observed at H_c. Above H_c the saturated paramagnetic state with near fully saturated moment is induced. Since a pronounced drop of the resistivity at H_c sharpens as temperature decrease, the transition associated with the MMT may well be first order below 0.4 K. In Ref. 10 the phase diagram based on polycrystalline samples indicates three distinct magnetic phase boundaries. The two phase boundaries between regions I, II, and III in Ref. 10 are consistent with the phase lines for $\mathbf{H}\|\mathbf{a}$ in this study. However, the third phase boundary between region III and paramagnetic phase in Ref. 10 is not present in Fig. 11. From a simple point of view, since $CeNiGe_3$ is highly magnetically anisotropic, the third phase boundary seen in the polycrystalline samples may primarily reflect that for the magnetic hard axis **b** or **c**. We have been measured $\chi(T)$ for magnetic field applied along magnetic hard axes (see Fig. 2). For $H=70$ kOe, $\chi(T)$ reveals a shift of the AFM ordering temperature from 5.0 to 4.2 K for $\mathbf{H}\|\mathbf{b}$ and to 4.9 K for $\mathbf{H}\|\mathbf{c}$, which is close to the third phase boundary in Ref. 10. The constructed H-T phase diagram for $\mathbf{H}\|\mathbf{a}$ is qualitatively in agreement with the phase diagram from previous polycrystalline sample study.[10] Hence, although polycrystalline samples can show intrinsic property of materials with directional averaged value, single crystals are needed for reliable H-T phase diagrams of magnetically anisotropic compounds.

$CeNiGe_3$ manifests a large magnetic anisotropy and the specific heat shows a broad peak centered around 45 K in zero field, both of which are presumably associated with the CEF splitting of the Ce Hund's rule ground state multiplet. In order to better understand the salient energy scales for this

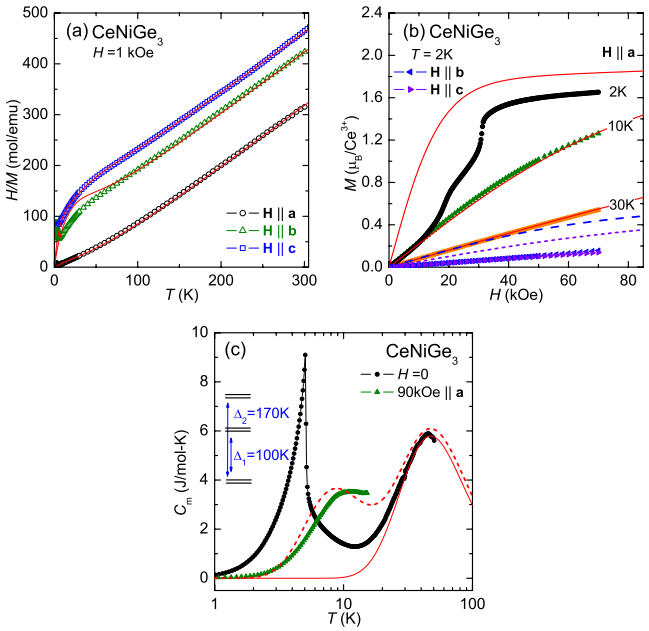

FIG. 12. (Color online) (a) Inverse magnetic susceptibility (open symbols) and calculated curves based on the CEF model (solid lines). (b) Magnetization isotherms for **H**∥**a** (2, 10, and 30 K), **H**∥**b** (2 K), and **H**∥**c** (2 K). Solid lines are the calculated curves based on the CEF model for **H**∥**a** and T=2, 10, and 30 K. Dashed (dotted) line is the calculated curve for **H**∥**b** (**H**∥**c**). (c) Magnetic specific heat at H=0 and 90 kOe. Solid and dashed lines are the calculated magnetic specific heat curves based on the CEF model at H=0 and 90 kOe, respectively, for **H**∥**a**. The given energy-level scheme, shown on the left side, represents that the first and second excited state energy levels of the Kramers doublets are separated by $\Delta_1 \sim 100$ K and $\Delta_2 \sim 170$ K, respectively, from the ground-state doublet.

system, these data were analyzed on the basis of the CEF (point charge) model. The CEF Hamiltonian for the Ce^{3+} ion (J=5/2) in orthorhombic point symmetry can be written as $H_{CEF}=B_2^0O_2^0+B_2^2O_2^2+B_4^0O_4^0+B_4^2O_4^2+B_4^4O_4^4$. Where O_m^n and B_m^n are Steven's operators and CEF parameters, respectively.[26,27] In the paramagnetic state, the magnetic properties of the material are determined by CEF plus Zeeman interaction ($H_Z = g\mu_B JH$), thus the total Hamiltonian $H=H_{CEF}+H_Z$ was used for the analysis of the present data.

The CEF parameters were determined by reproducing the measured specific heat, magnetic susceptibility, and magnetization isotherms with calculated curves shown as solid line in Fig. 12. The obtained CEF parameters and the CEF level scheme are summarized in Table I and the zero field energy level scheme is shown in Fig. 12(c). In the paramagnetic state, $\chi(T)$ and $M(H)$ are satisfactorily reproduced by the calculated values as shown in Figs. 12(a) and 12(b). Although $M(H)$ data at 2 K are not exactly reproduced, the anisotropy between **H**∥**a** and **H**∥**b** and **c** is reasonable. The two MMTs, of course, are not captured by single ion, CEF effect. Thus, in addition to the CEF effect, other interactions should be taken into consideration to reproduce the MMT behavior in $CeNiGe_3$. In similar manner, the magnetic ordering seen as a λ-like anomaly in the zero field C_p is not captured in the CEF model, but the high-field splitting of the ground state doublet is. At high temperatures C_m is well reproduced by the CEF model as shown in Fig. 12(c). The energy-level splitting Δ_1=100 K from the ground state doublet to the first excited doublet is consistent with the entropy change shown in Fig. 4. Furthermore, for H=90 kOe, the low-temperature broad peak is reproduced, giving rise to a split of ground state double via Zeeman interaction.

Turning now to the low-temperature resistivity, it is expected that FL behavior should be recovered for $H>H_c$. Figure 13 shows that, for selected magnetic fields, $\rho(T)$ for $CeNiGe_3$ varies as $\rho(T)=\rho_0+AT^n$ with $n\geq 2$ below 2 K. The vertical arrow in Fig. 13(a) indicates the onset of AFM order, below which a small enhancement of $\rho(T)$ is observed rather than a drop due to the loss of spin disorder scattering. As magnetic field increases from 32.25 to 32.75 kOe the AFM order is fully suppressed. In the vicinity of the AFM to paramagnetic (PM) phase boundary a quadratic temperature dependence in $\rho(T)$ emerges [see Fig. 13(b)]. A FL behavior, n=2, is obtained just above H_c, but only over a limited range of temperature and magnetic field. At low temperatures,

TABLE I. CEF parameters, energy levels, and wave functions in $CeNiGe_3$.

CEF parameters (K)					
B_2^0	B_2^2	B_4^0	B_4^2	B_4^4	
5.36	−11.15	0.12	0.58	1.02	
Energy levels and wave functions					
E (K)	$\lvert+\frac{5}{2}\rangle$	$\lvert+\frac{3}{2}\rangle$	$\lvert+\frac{1}{2}\rangle$	$\lvert-\frac{1}{2}\rangle$	$\lvert-\frac{3}{2}\rangle$	$\lvert-\frac{5}{2}\rangle$
171.7	0.848	0	−0.357	0	0.391	0
171.7	0	−0.393	0	0.358	0	−0.847
99.3	−0.527	0	−0.635	0	0.565	0
99.3	0	−0.564	0	0.634	0	0.529
0	0	−0.726	0	−0.685	0	0.047
0	0.047	0	0.685	0	0.726	0

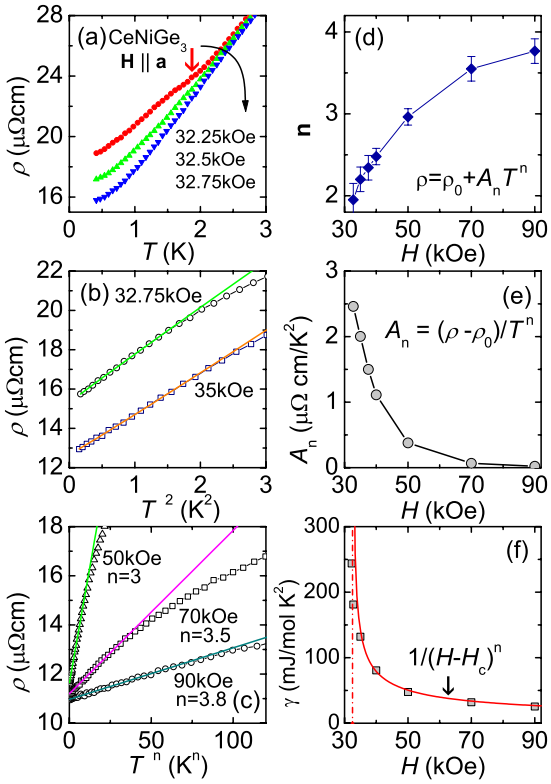

FIG. 13. (Color online) (a) Low-temperature electrical resistivity at 32.25, 32.5, and 32.72 kOe for **H**∥**a**. Vertical arrow indicates the onset of the AFM phase transition. (b) Resistivity as a function of T^2 for $H=32.75$ and 35 kOe. (c) Resistivity as a function of T^n, $\rho(T)=\rho_0+A_nT^n$, at $H=50$ kOe ($n=3$), 70 kOe ($n=3.5$), and 90 kOe ($n=3.8$). (d) Exponent n (e) coefficient A_n as a function of magnetic field. (f) C_m/T at $T=0.4$ K (inset, Fig. 5). The solid line represents a fit of the equation, $C_m/T \propto 1/(H-H_c)^{\beta}$, performed between 35 and 90 kOe with $n=0.52$ and $H_c=32.5$ kOe. The vertical dashed-dotted line indicates H_c.

$H>H_c$, $\rho(T)$ displays an anomalous T^n dependence with $n>2$, indicative of deviation from FL behavior, as shown in Fig. 13(c). This suggests that an additional scattering mechanism in $\rho(T)$ needs to be considered in the saturated paramagnetic (spin-polarized) states. The exponent, n, gradually increases as magnetic field increases, reaching $n=3.8$ at $H=90$ kOe [Fig. 13(d)], where the coefficient, $A_n=[\rho(T)-\rho_0]/T^n$, corresponding to each n is plotted in Fig. 13(e). The A_n value quickly drops with increasing magnetic fields for $H>H_c$.

In general, when T_N, tuned by external magnetic field, is suppressed to $T\rightarrow 0$, pronounced nFL properties are observed in the vicinity of QCP in HF AFM systems such as $YbRh_2Si_2$,[4,5] $CeAuSb_2$,[6] and YbAgGe.[7–9] For $CeNiGe_3$ there is no clear indication of nFL behavior, $\Delta\rho=AT^n$ with $n<2$ and $C/T\propto -\log(T)$, in the vicinity of H_c down to 0.4 K. Therefore, although the AFM order in $CeNiGe_3$ can be suppressed by an applied magnetic field, a classical QCP is not obtained as $T_N\rightarrow 0$. This may arise due to a weak hybridization between $4f$ and conduction electrons and the possible first order nature of this phase transition for $T<0.4$ K and $H\sim H_c$, i.e., Ce in this system is much more local moment like and the H-T phase diagram is closer to nonhybridizing rare earth such as $RAgSb_2$ or $RAgGe$ system (R =rare earth).[28,29] For many field-tuned QCP systems,[3,4,6] when approaching the QCP from the paramagnetic state, the coefficient A of the T^2 dependence of resistivity has a $1/(H-H_c)^{\beta}$ scaling form, where H_c is the critical field and β is the exponent. Since $\rho(T)$ of $CeNiGe_3$ shows a T^2 dependence only over a limited temperature and field range, this scaling property cannot be tested in this system. Interestingly, however, a $1/(H-H_c)^{0.52}$ divergence for $H>H_c$ is observed from the field dependence of C_m/T at 0.4 K. The solid line in Fig. 13(f) represents a fit of the scaling form performed for $H\geq 35$ kOe with $H_c=32.5\pm 0.5$ kOe and $\beta=0.52\pm 0.1$, implying a divergence of the quasiparticle mass approaching H_c. By assuming $A\propto\gamma^2$ (Ref. 30) holds in the paramagentic state, this implies that the field dependence A can show a singular scattering near H_c following $\sim 1/(H-H_c)$. In order to address this issue, it will be necessary to measure the resistivity below 0.4 K. It is interesting to note that the $n>2$ deviation from FL behavior is also seen in $CeAuSb_2$ (Ref. 6) and $YbNiSi_3$.[16] Both compounds show very similar H-T phase diagrams with two MMTs, emerging when T_N is lowered by applied magnetic field. The observed MR response through the MMTs is also quite similar. The anomalous metallic behavior in the saturated paramagnetic state induced by magnetic field is reflected by T^3 dependence for $CeAuSb_2$ and T^n with $n>2$ for $YbNiSi_3$ at low temperatures.

V. SUMMARY

We have studied the thermal, magnetic, and electrical properties of the single crystals of $CeNiGe_3$ by means of the specific heat, magnetization, and electrical resistivity. $CeNiGe_3$ manifests a large magnetic anisotropy with the crystallographic **a** axis being the magnetic easy axis. In the paramagnetic phase, the observed behavior can be well explained by the CEF effect with an ~ 100 K splitting between the ground-state doublet and the first excite state. The low-temperature physical properties manifest strong magnetic field dependencies. The constructed H-T phase diagram indicates that the AFM order can be suppressed by magnetic field of $H_c=32.5$ kOe to $T=0$ through MMT. No clear indication of nFL behavior was observed in the vicinity of the H_c. A FL behavior close to the H_c is found over a limited range of temperature and magnetic field. At higher fields an anomalous temperature dependence of the resistivity was observed.

ACKNOWLEDGMENTS

We would like to thank Hyunjin Ko for single crystal x-ray measurements. Work at Ames Laboratory was supported by the Basic Energy Sciences, U.S. Department of Energy under Contract No. DE-AC02-07CH11358.

[1] A. C. Hewson, *The Kondo Problem to Heavy Fermions* (Cambridge University Press, Cambridge, 1993).
[2] See, for example, G. R. Stewart, Rev. Mod. Phys. **78**, 743 (2006); **73**, 797 (2001).
[3] H. v. Löhneysen, A. Rosch, M. Vojta, and P. Wölfle, Rev. Mod. Phys. **79**, 1015 (2007).
[4] P. Gegenwart, J. Custers, C. Geibel, K. Neumaier, T. Tayama, K. Tenya, O. Trovarelli, and F. Steglich, Phys. Rev. Lett. **89**, 056402 (2002).
[5] J. Custers, P. Gegenwart, H. Wilhelm, K. Neumaier, Y. Tokiwa, O. Trovarelli, C. Geibel, F. Steglich, C. Pépin, and P. Coleman, Nature (London) **424**, 524 (2003).
[6] L. Balicas, S. Nakatsuji, H. Lee, P. Schlottmann, T. P. Murphy, and Z. Fisk, Phys. Rev. B **72**, 064422 (2005).
[7] S. L. Bud'ko, E. Morosan, and P. C. Canfield, Phys. Rev. B **69**, 014415 (2004).
[8] P. G. Niklowitz, G. Knebel, J. Flouquet, S. L. Bud'ko, and P. C. Canfield, Phys. Rev. B **73**, 125101 (2006).
[9] Y. Tokiwa, A. Pikul, P. Gegenwart, F. Steglich, S. L. Bud'ko, and P. C. Canfield, Phys. Rev. B **73**, 094435 (2006).
[10] A. P. Pikul, D. Kaczorowski, T. Plackowski, A. Czopnik, H. Michor, E. Bauer, G. Hilscher, P. Rogl, and Yu. Grin, Phys. Rev. B **67**, 224417 (2003).
[11] O. I. Bodak, V. K. Pecharskii, O. Ya. Mruz, V. E. Zavodnik, G. M. Vitvitskaya, and P. S. Salamakha, Dopov. Akad. Nauk Ukr. RSR, Ser. B: Geol., Khim. Biol. Nauki **2**, 36 (1985).
[12] H. Ko, Ph.D. thesis, Iowa State University, 2008.
[13] M. Nakashima, K. Tabata, A. Thamizhavel, T. C. Kobayashi, M. Hedo, Y. Uwatoko, K. Shimizu, R. Settai, and Y. Ōnuki, J. Phys.: Condens. Matter **16**, L255 (2004).
[14] H. Kotegawa, K. Takeda, T. Miyoshi, S. Fukushima, H. Hidaka, T. C. Kobayashi, T. Akazawa, Y. Ohishi, M. Nakashima, A. Thamizhave, R. Settai, and Y. Ōnuki, J. Phys. Soc. Jpn. **75**, 044713 (2006).
[15] N. Tateiwa, Y. Haga, T. D. Matsuda, S. Ikeda, M. Nakashima, A. Thamizhavel, R. Settai, and Y. Ōnuki, J. Phys. Soc. Jpn. **75**S, 174-176 (2006).
[16] S. L. Bud'ko, P. C. Canfield, M. A. Avila, and T. Takabatake, Phys. Rev. B **75**, 094433 (2007).
[17] Z. Fisk and J. P. Remeika, in *Handbook of Physics and Chemistry of Rare Earths*, edited by K. A. Gschneidner and L. R. Eyring (North-Holland, Amsterdam, 1989), Vol. 12, p. 53.
[18] P. C. Canfield and Z. Fisk, Philos. Mag. B **65**, 1117 (1992).
[19] P. C. Canfield and I. R. Fisher, J. Cryst. Growth **225**, 155 (2001).
[20] M. E. Fisher, Philos. Mag. **7**, 1731 (1962).
[21] M. E. Fisher and J. S. Langer, Phys. Rev. Lett. **20**, 665 (1968).
[22] M. Bouvier, P. Lethuillier, and D. Schmitt, Phys. Rev. B **43**, 13137 (1991).
[23] J. A. Blanco, D. Gignoux, and D. Schmitt, Phys. Rev. B **43**, 13145 (1991).
[24] K. D. Schotte and U. Schotte, Phys. Lett. A **55**, 38 (1975).
[25] R. A. Ribeiro, S. L. Bud'ko, and P. C. Canfield, J. Magn. Magn. Mater. **267**, 216 (2003).
[26] K. W. H. Stevens, Proc. Phys. Soc., London, Sect. A **65**, 209 (1952).
[27] M. T. Hutchings, in *Solid State Physics: Advances in Research and Applications*, edited by F. Seitz and D. Turnbull (Academic, New York, 1964), Vol. 16, p. 227.
[28] K. D. Myers, S. L. Bud'ko, I. R. Fisher, Z. Islam, H. Kleinke, A. H. Lacerda, and P. C. Canfield, J. Magn. Magn. Mater. **205**, 27 (1999).
[29] E. Morosan, S. L. Bud'ko, P. C. Canfield, M. S. Torikachvili, and A. H. Lacerda, J. Magn. Magn. Mater. **277**, 298 (2004).
[30] K. Kadowaki and S. B. Woods, Solid State Commun. **58**, 507 (1986).